Imprinted cell memory in glycogen storage disorder 1a

Sprecher U** [1], D'Souza J** [1], Mishra K [2,3], Canella Miliano A [4], Mithieux G [4], Rajas F [4], Avraham S [5], Anikster Y [6,7], Kakhlon O* [2,3], and Weil M* [1]

*Corresponding authors

**Equal contribution

1. The Shmunis School of Biomedicine and Cancer Research, The George S. Wise Faculty for Life Sciences, Sagol School of Neurosciences, Tel Aviv University, 6997801 Tel Aviv, Israel.

2. Department of Neurology, Hadassah-Hebrew University Medical Center, Ein Kerem, Jerusalem 9112102, Israel.

3. Faculty of Medicine, Hebrew University of Jerusalem, Ein Kerem, Jerusalem 9112102, Israel.

4. Universite Claude Bernard Lyon 1, Universite de Lyon, INSERM UMR-S1213, Lyon, France.

5. Department of Chemistry, Raymond and Beverly Sackler Faculty of Exact Sciences, Department of Biomedical Engineering, School of Chemistry, Tel Aviv University, 6997801 Tel Aviv, Israel

6. Edmond and Lily Safra Children's Hospital, Sheba Medical Center Tel-Hashomer 52621, Israel

7. Sackler School of Medicine, Tel Aviv University, 6997801 Tel Aviv, Israel

Summary

Glycogen storage disorder type 1a (GSD1a) is caused by loss-of-function mutations in the catalytic subunit of glucose-6-phosphatase enzyme (*G6PC1*) in the liver, kidney and intestine exclusively. Here we show the surprising results that while not expressing *G6PC1*, primary skin fibroblasts isolated from GSD1a patients' skin biopsies preserve a distinctive disease phenotype irrespective of the different culture conditions under which they grow. This discovery was initially made by phenotypic image-based high content analysis (HCA). Deeper analysis into this disease phenotype, revealed impaired lysosomal and mitochondrial functions in GSD1a cells, which were driven by a transcriptional dysregulation of the NAD^+/NADH-Sirt1-TFEB regulatory axis. This dysregulation impacts the normal balance between mitochondrial biogenesis and mitophagy in the patients' cells. The distinctive GSD1a fibroblasts phenotype involves elevated H3 K27 histone acetylation and global DNA hypomethylation suggesting that in some way the disease imprinted a distinctive cell phenotype in these cells. Remarkably, GHF201, an established glycogen reducing molecule, which ameliorated GSD1a pathology in a liver-targeted inducible *L.G6pc*$^{-/-}$ knockout mouse model, also reversed impaired cellular functions in GSD1a patients' fibroblasts. Altogether, this experimental evidence strongly suggests that these cells express a strong and reversible disease phenotype without expressing the causal *G6PC1* gene.

Introduction

Glycogen storage disorder type 1a (GSD1a), or von Gierke disease, is caused by deficiency in glucose-6-phosphatase (G6Pase) activity, which catalyzes the hydrolysis of glucose-6-phosphate to glucose and phosphate in the terminal steps of gluconeogenesis, and glycogenolysis-dependent glucose production in the kidney, intestine, and liver exclusively [1], [2], [3], [4], [5]. GSD1a is a rare disease within the group of glycogen storage disorders (GSDs) that are inherited diseases of glycogen metabolism where either the breakdown or synthesis of glycogen is disturbed. There are 19 types of GSDs [6], and they are classified based on the enzyme deficiency and the affected tissue [7]**.** GSD1a is characterized by accumulation of glycogen and fat in the liver and kidneys, resulting in hepatomegaly, renomegaly, signs of hypoglycemia, growth failure, as well as hyperlipidemia, hypercholesterolemia, hyperlactatemia and hyperuricemia [8], [9],[10]. Currently there is no cure for GSD1a. Treatment is limited to dietary interventions alone which may hold off some of the disease symptoms[11]. Since glycogen accumulation is the pathogenic factor in glycogen storage disorders, we have previously developed a cell-based assay for drug high throughput screening (HTS) to identify small molecule inhibitors of polyglucosan bodies (PGB) accumulation, irrespective of the mechanism of their formation, in skin fibroblasts of patients with Adult Polyglucosan Body Disease APBD, or GSD type IV [12]. One of these compounds has so far shown positive results in an APBD mouse model with significant improvement in survival, metabolism and mitigation of disease

progression [13]. Remarkably, the lysosomal protein LAMP1 was demonstrated to be the target of this compound, named GHF201, improving the impaired autophagic flux, as well as mitochondrial activity in APBD patients' fibroblasts [13]. In our efforts to evaluate GHF201 as a potential global therapeutic agent for GSDs, we opted to first characterize GSD1a patients' primary fibroblasts phenotype as a cell model for the disease, using image-based high content analysis (HCA) as done previously for APBD fibroblasts, but having in mind that the G6PC1 encoding gene *G6PC1* is not expressed in fibroblasts [14]. We hypothesized that under these circumstances GSD1a patients' fibroblasts can serve as a useful negative control to test tissue specific effects of the novel compound. Here we show the surprising results from phenotypic HCA experiments that GSD1a patients' fibroblasts have a distinctive disease phenotype as compared to healthy control (HC) fibroblasts. Key organelles such as mitochondria and lysosomes show the strongest morphometric differences in spite of the fact that *G6PC1* is not expressed in these cells. Deeper analysis into the GSD1a phenotype indicates a lower oxygen consumption rate (OCR) and poor ATP production by mitochondria and high glycolytic compensation in these cells. Also, lysosomal function and autophagy were compromised, and, expectedly, recovered by GHF201, in GSD1a fibroblasts. Furthermore, we show that PGC1α and TFEB [15], [16]. the transcriptional regulators of mitochondrial biogenesis and lysosomal function, respectively, and the major regulators of the metabolic axis pAMPK-SIRT1-NAD^+/NADH are significantly inhibited in GSD1a patients' fibroblasts. Moreover, the SIRT1-inhibitable histone H3K27 acetylation [17],[18]. was elevated in the chromatin of GSD1a patients' fibroblast and, in turn, reduced by GHF201 treatment. Importantly, the curative effect of GHF201 is not restricted to GSD1a patients' fibroblasts and it does ameliorate established GSD1a pathology by reducing liver G6P and glycogen and increasing liver and serum glucose in a liver-targeted inducible *L.G6pc*$^{-/-}$ knockout mouse model of GSD1a. Altogether, this experimental evidence describes a strong disease phenotype in GSD1a fibroblasts without expressing the *G6PC1* gene suggesting a disease imprinted phenotype caused by a yet not fully deciphered mechanism. Moreover, the beneficial GHF201 effects *in vitro* and *in vivo* may consolidate further its novel therapeutic potential for GSDs.

Results

The Phenotypic analysis of GSD1a fibroblasts by image-based HCA

To characterize the phenotype of skin fibroblasts from GSD1a patients we applied image-based HCA in several independent experiments. For this purpose, skin fibroblasts from GSD1a patients and HC (age and gender matched) individuals were incubated for 24 h and 48 h in cell culture media under serum and glucose starvation and for 72 h where full medium (with serum and glucose) was restored for the last 24 h

of incubation. These different culture conditions were used to induce metabolic stress in the cells caused by sugar deprivation (24 and 48 h) and consecutive glycogen burden caused by adding back sugar to the media for 24 h (72 h), which proved to be highly effective in describing the GSD phenotype as shown in similar, previously published HCA phenotyping experiments of APBD (GSD-IV) patients' fibroblasts [13]. At each experimental time point, the cells were simultaneously co-stained with fluorescent probes for nuclei, cytoplasm, lysosomes and active mitochondria. Live images were then taken and quantitatively analyzed. To simplify data representation by our image analysis software, we narrowed the number of features generated from cell images of 4 different cell compartments from ~150 down to 24 using feature selection by backward feature elimination (see Methods). The selected 24 features were represented by area (size of the organelle), fluorescence intensity, and texture (combines area and intensity). To statistically confirm the phenotypic differences, two-tailed t-tests were performed between GSD1a and HC samples for each condition (24, 48 and 72 h), and each feature (area, fluorescence intensity and texture) for each labeled organelle: mitochondria, lysosome, cytoplasm, and nucleus (Supplementary Table 1). Figure 1a shows representative images of GSD1a and HC labeled fibroblasts stained with the 4 different live dyes. Box-plots of selected features representing texture of TMRE (active mitochondria), lysotracker (lysosomes) and calcein-AM (cytoplasm) and the area feature for Hoechst (nuclei) are shown in Figure 1b for all tested conditions. These features were arbitrarily selected from the statistical analysis mentioned above (Supplementary Table 1) to simplify the existing phenotype differences between the groups in Figure 1. Our results indicate significant differences between GSD1a and HC samples, such as smaller nucleus areas (Hoechst) and lower textures of active mitochondria (TMRE), lysosomes (lysotracker) and cytoplasm (calcein-AM) in the GSD1a samples compared to HC. Scatter plots for each of the labeled organelle features were generated (Figure 1b, bottom) to strengthen the statistical analysis visualization, showing the levels of the selected features in each condition. The shade overlapping each line represents a 90 percent confidence interval which allows us to see that there is almost no overlap between the GSD1a and HC samples in all time conditions. These results suggested a strong cell phenotype in GSD1a fibroblasts that is different from HC regardless of the experimental conditions. This conclusion was confirmed by a heatmap analysis of the 24 selected features, showing the area, intensity and texture for all 4 labels in cells (Figure 1c). Principal component analysis (PCA) of the data from all the features per sample for each condition is shown in Figure 1d. The PCA shows that the overall variance explained by PC1 (55% of total variance) shows a clear separation between HC and GSD1a fibroblasts. The PC2 (24% of total variance) shows that there is also a clear separation between the different culture conditions – 24, 48 and 72 h - indicating a clear phenotypic difference between the starvation and serum restoration conditions, where GSD1a fibroblasts respond differently to the medium conditions than HC fibroblasts. To further differentiate between our GSD1a and HC samples and for

better insight into the main features that contribute to the phenotypic group separation, we performed linear discriminant analysis (LDA) on our data (Figure 1e). The LDA algorithm presented a clear separation between HC and GSD1A samples by LD1 (92% of total variance) showing that the top contributors to variation are active mitochondria, lysosomes, cytoplasm, and nuclei features (see Supplementary Figure 1 for features most contributing to phenotypic separation which were used in Figure 1c). These results showcased a strong image-based phenotype of the GSD1a cells in all culture conditions. Nevertheless, the 72 h culture condition showed the most compelling differences between the groups. For this reason, our further study into the GSD1a phenotype shown below was done at this condition. Moreover, the results indicate that the affected organelles found in these experiments align well with known results from other more established GSD1a models *in vivo* and *in vitro*, showing impaired mitochondrial and lysosomal pathways [19], [20], [21], [3], [22].

The mitochondrial function of GSD1a fibroblasts and its modulation by GHF201

To further characterize the mitochondrial and lysosomal phenotype of GSD1a fibroblasts, deeper phenotypic and functional analysis of the GSD1a mitochondrial and lysosomal differences from HC was performed in patients' skin fibroblasts in the presence or absence of our newly discovered GHF 201 compound. Recently, we identified LAMP1 as the specific target and mode of action of this glycogen reducing compound in fibroblasts from APBD patients, where GHF201 also alleviated compromised mitochondrial and autophagy functions [13]. As a first step, we confirmed the effect of GHF201 on glycogen reduction in GSD1a fibroblasts by Periodic acid–Schiff (PAS) assay (see Supplementary Figure 2). Mitochondrial activity in GSD1a fibroblasts, as compared to HC, is compromised in all the parameters derived from the oxygen consumption rate (OCR) as demonstrated in our Seahorse extracellular flux experiments (Figure 2a): Basal and maximal respiration rates were lower in GSD1a cells compared with HC (Figure 2b, c). Furthermore, ATP production, spare respiratory capacity, proton leak and non-mitochondrial respiration rates were also significantly lower in GSD1a cells compared with HC (Figure 2d-g). GHF201 treatment significantly increased all these OCR-derived parameters (Figure 2a-g). We hypothesized that the deficient ATP production observed in these experiments may have stimulated glycolytic compensation in GSD1a cells. To test this possibility, we performed Seahorse's real-time ATP rate assay to simultaneously quantify ATP production from glycolysis and OxPhos. GlycoATP production in GSD1a cells was significantly decreased, while mitoATP production rate wasn't altered as compared to HC (Figure 2h). GHF201 increased the relative contribution of glycolytic ATP production at the expense of mitochondrial (OxPhos) ATP production in HC but not in GSD1a cells. Acute on-assay supplementation of GHF201 for 20 minutes was more effective at augmenting the glycolytic contribution to ATP production than 24 h (chronic) pretreatment with GHF201 in HC

compared to GSD1a cells (Figure 2h). This can be explained by the extracellular acidification rate results showing a higher dependency on glycolysis in GSD1a cells throughout the assay (Figure 2i) indicated by higher glycolysis and glycolytic capacity (Figures 2j, k) with or without GHF201.

The lysosomal pathway in GSD1a fibroblasts and its targeting by GHF201

To confirm that the differences in lysosomal morphology associated with the diseased state (Figure 1) also have a functional manifestation, we measured by flow cytometry lysosomal pH using the ratiometric dye lysosensor, which quantifies pH based on the 375 nm-excited yellow/blue emission ratio. Our results (Figure 3a) show that lysosomes in GSD1a fibroblasts are more alkaline than lysosomes in HC fibroblasts. Moreover, in agreement with our previous results in APBD fibroblasts[12], GHF201 acidified lysosomes in both HC and GSD1a fibroblasts, suggesting improvement of lysosomal function. Next, to investigate the implications of this phenotype on autophagy, we performed experiments aimed at determining the autophagic flux in GSD1a patient cells by Western blot analysis. Our results show that GHF201 increased the sensitivity of the LC3II/LC3I ratio to the lysosomal inhibitor vinblastine. As shown in Figure 3c, the vinblastine-dependent increase in the LC3II/LC3I ratio (i.e., autophagic halt) was further increased by GHF201 in GSD1a cells. GHF201-dependent increase in autophagic flux is also manifested by reduction in the levels of the autophagy substrate p62 (Figure 3c and representative images in Supplementary Figure 3). Moreover, stronger evidence for deficient autophagic regulation in GSD1a patient cells is demonstrated by lower levels of the transcription factor TFEB in the cell nuclei as determined by image HCA using an anti-TFEB antibody (Figure and representative images in Supplementary Figure 3). Altogether these results strongly suggest that GSD1a patient fibroblasts express an endogenous disease phenotype regardless of the fact that the mutated *G6PC1* gene is not expressed in these cells.

Elucidating the metabolic regulators of the GSD1a phenotype

To try and solve this apparent paradox (presence of a phenotype *vis a vis* absence of a mutation), we hypothesized that epigenetic changes may be responsible for the GSD1a phenotype in skin fibroblasts and performed further studies related to the putative epigenetic molecular pathway as shown in Figure 4. This pathway is triggered by phosphorylation of AMPK, which is low in GSD1a cells, compared to HC, as shown by IF HCA (Figure 4a and representative images in Supplementary Figure 3). p-AMPK-mediated activation in turn up-regulates the mitochondrial respiration-dependent NAD^+/NADH ratio, which is reduced in GSD1a (see Figure 4b). The NAD^+/NADH ratio correlates with the mitochondrial respiration rate as NADH is oxidized by complex I. This is also shown in our bioenergetic results, where HC cells

with higher NAD^+/NADH also manifest higher mitochondrial respiration (Figure 2). However, the biological significance of increased respiration is not necessarily an increase in ATP availability, due to the increased respiration, and ATP is not always a limiting factor for cell thriving. As stated, increased mitochondrial respiration also increases NAD^+ availability, which plays a major role in glycolysis, TCA cycle, and amino acid, fatty acid and nucleotide synthesis [23]. To test the relative contribution of NAD^+ *v* ATP to cell thriving, we imposed ATP demand using the cation ionophore gramicidin, which induces ATP turnover to activate the Na/K pump and restore intracellular ion concentration gradients. Increased ATP turnover and ADP/ATP ratio by gramicidin elevated the NAD^+/NADH ratio probably by activation of F1F0-ATPase and consequent dissipation of the mitochondrial membrane proton gradient (Figure 4c). This NAD^+/NADH increase correlated with reduced cytotoxicity and increased cell confluence (Figure 4d) suggesting that NAD^+ availability prevails over ATP availability as an effector of cell thriving in GSD1a cells. GHF201, both on its own and in combination with gramicidin, also increased NAD^+/NADH and cell viability, which was reversed by the respiration inhibitor oligomycin A, in further support that respiration-dependent NAD^+ availability mediate GHF201's corrective effect in GSD1a cells. The GHF201-mediated increase in NAD^+ is especially interesting considering that the level of the NAD^+-dependent histone deacetylase Sirt1 was reduced in GSD1a cells (Figure 4e and representative images in Supplementary Figure 3). Sirt1 has a critical and specific epigenetic effect on the chromatin, which is deacetylation of Histone 3 at the lysine 27 acetylation site in the chromatin [17], [18]. Our results show increased acetylation of H3K27 in GSD1a as compared to HC and reversal of this acetylation by GHF201 (Figure 4f). Note that in HC cells, initially showing low H2K27 acetylation, GHF201 effect was less pronounced as in GSD1a. This increased histone acetylation might be linked to the observed inhibition of Sirt1 in GSD1a cells, and its reversal might be due to reactivation of Sirt1 by the GHF201-mediated increase in NAD^+ availability (Figure 4c). Moreover, the global pattern of non-methylated regions of genomic DNA in the GSD1a and HC groups was determined by SIGL (see Methods). Our results show reduced unmodified methylated CpG regions in the HC cells indicating relatively higher levels of DNA methylation in GSD1a fibroblasts (see Supplementary Figure 4). To further investigate the implications of this regulatory pathway with respect to mitochondrial biogenesis and homeostasis in the GSD1a phenotype, we looked into the expression of the transcription factor PGC1α levels (Figure 5a and representative images in Supplementary Figure 3), which are lower in GSD1a cells, as compared to HC, and which can be increased by GHF 201 treatment. Following these results, we tested the protein levels of the PGC1α dependent regulators of mitochondrial biogenesis [24, 25, 26]. NRF1 and TFAM and of the positive regulator of the mitochondrial electron transfer chain cytochrome oxidase IV (COX IV) in GSD1a patients' cells. Our WB data (Figure 5b) indicate that the expression levels of each of the mitochondrial biogenesis markers NRF1, TFAM, and of the ETC regulator COX IV are significantly

lower in GSD1a fibroblasts than in HC fibroblasts. Interestingly, treatment with GHF201 shows an increasing effect on the levels of these markers. Moreover, we performed studies using GSD1a and HC cells stably expressing the mCherry-GFP-FIS1-leading-sequence plasmid (mCherry–GFP tag attached to the outer mitochondrial membrane localizing signal of the FIS1 protein (residues 101–152)) to show mitophagy activity [27], which selectively removes and recycles dysfunctional and cell-damage propagating mitochondria (see Methods). The results show that mitophagy is significantly impaired in the GSD1a cells demonstrated by lower mCherry/(mCherry+GFP) intensity ratio compared to HC while GHF201 treatment manages to increase this ratio (Figure 5c). Altogether, these experiments strongly suggest that mitochondrial biogenesis is one of the factors involved in the abnormal mitochondrial phenotype and function in GSD1a cells. Interestingly, GHF201 increased mitochondrial biogenesis markers and improved mitochondrial function in GSD1a cells, which in turn may have a beneficial effect on mitochondrial homeostasis.

The interaction between multiple phenotypic features in GSD1a fibroblasts

To analyze the extent of the GSD1a phenotype in patients' primary fibroblasts and GHF201's impact on it, we performed an integrative analysis of representative features of our multilevel phenotypic results shown in Figures 1-5 (see Figure 6). First, we performed a correlation analysis using the Pearson test between different representative features (Lyso intensity, Lyso Area, TMRE intensity, Nuc area, Sirt-1, autophagy flux, PGC1α, TFEB, p62 and COX IV) from HCA and biochemical analysis of both the GSD1a (n=3) and HC (n=3) groups. These features were chosen based on their biological importance considering their potential interaction due to their respective role in the cell. Figure 5a shows the correlation index among all these ten features graded by a color scale. These results confirm that the phenotypic differences between GSD1a and HC, observed in lysosomes, mitochondria and nuclei, are linked to the key biochemical marker or pathway found to be involved in the disease phenotype. For instance, autophagic flux is highly (inversely) correlated with p62 intensity (Pearson coefficient = -0.92), but not significantly correlated with nuclear (Hoechst) area (Pearson coefficient = -0.12). Next, we determined cluster differences between the groups HC (n=3), GSD1a (n=3) and GSD1a treated with GHF201 (n=3) by unsupervised K-means analysis of the relevant biochemical data (AMPK, Sirt-1, NAD/NADH, TFEB, Autophagy FLUX, p62, PGC1α, NRF1, COX IV, Seahorse-BASAL,-maximal, -ATP) produced from the above mentioned experiments to test these integrated data for group classification of each sample (Figure 6b). A 95 percent confidence interval was obtained for each group cluster formed by 3 individual fibroblasts samples. Interestingly, GHF 201 treatment positions the GSD1a fibroblasts data cluster closer to the HC cluster than to the GSD1a (DMSO) cluster suggesting that GHF201 treatment brings the GSD1a biochemical pathways closer to HC, which implies a curative effect.

We then investigated if the integration of GSD1a pathways and phenotype with concomitant GHF201 treatment is consistent with the known molecular relationship [28], [29], [30], [31] between the different pathways and phenotypes in the untreated fibroblasts. Figure 6c shows the network analysis of the interaction between the key markers and their representative size before and after GHF 201 treatment to represent the main phenotypic pathways in a more simplified manner. Overall, it is clear that there are differences between the node sizes in GSD1a untreated (DMSO) and treated (GHF 201) networks. Importantly, the metabolic regulator Sirt-1 pathway, dependent on NAD^+ availability, is clearly upregulated in the presence of GHF201 which impacts on both the mitochondrial and lysosomal branches. Knowing that GHF201 targets the lysosomal marker LAMP-1 and in turn reduces glycogen accumulation (see difference in glycogen metabolite node size between groups) it becomes apparent that the compound's effect is mostly associated with the lysosomal-autophagy axis as previously demonstrated in APBD models [13]. This autophagy promoting activity might directly increase the ETC rate and ATP production, which in turn improves NAD^+/NADH ratio (see Figure 4) activating Sirt-1 deacetylase activity in the GSD1a disease phenotype. While this compelling evidence describes a clear GSD1a phenotype in patients' primary fibroblast with or without GHF201 treatment, to establish therapeutic relevance to GSD1a, there is a need to verify GHF201 treatment effects *in vivo* in a GSD1a mouse model.

GHF201 effect on GSD1a modeling L.G6pc$^{-/-}$ mice

To test the *in vivo* efficacy of GHF201, we used the *L.G6pc$^{-/-}$* liver-targeted inducible *G6pc1* knockout mouse model of GSD1a [32]. Following tamoxifen-induction of *G6pc1* knockout, mice were treated or not with GHF201 for 4 weeks (Figure 7a). Our results show that GHF201 treatment reduced liver G6P (Figure 7b, $p<0.007$) and glycogen (Figure 7c $p<0.1$) and increased glucose levels in liver (Figure 7d $p<0.03$). Interestingly, blood glucose levels were increased by GHF201 (Figure 7e). Hepatomegaly, or increase in liver weight in the tamoxifen-induced *L.G6pc$^{-/-}$* mice, wasn't corrected by GHF201 (Figure 7f). All these results point to direct therapeutic effects of GHF201 in this murine GSD1a model: GSD1a is characterized by accumulation of G6P and glycogen in the liver causing hepatomegaly and, most important clinically, hypoglycemia. Therefore, all these pathogenic factors were corrected *in vivo* by GHF201 suggesting a hepato-therapeutic effect *in vivo*.

Discussion

Here we present important evidence from deep phenotypic analysis of GSD1a patients' fibroblasts which demonstrates that these cells express a specific disease phenotype even though G6Pase, the liver enzyme

whose deficiency causes the GSD1a disease, is not expressed in these cells. This phenomenon reveals for the first time the possibility that somatic cells, whether originated from the affected tissue or not, maintain a disease phenotype, even when kept under standard culture conditions remote from the original pathological environment. At this point, we have not yet identified the exact signal from the organism, nor the imprinting mechanism responsible for the GSD1a fibroblasts phenotype. We are aware that this cell memory imprinting mechanism is different from the better described genomic or behavioral imprinting concepts [33], [34].

Our experimental evidence demonstrates that GSD1a patients' fibroblasts behave like diseased cells and respond to glycogen-reducing agents accordingly without the enzyme deficiency responsible for the disease. Image-based HCA experiments of GSD1a phenotype and deeper phenotypic analysis indicate impaired lysosomal and mitochondrial functions in GSD1a cells compared to HC, which is driven by a transcriptional dysregulation of the NAD^+/NADH-Sirt1-TFEB regulatory axis (Figure 6). This dysregulation impacts the normal balance between mitochondrial biogenesis and mitophagy as suggested by the changes in the levels of the mitochondrial biogenesis factors PGC1α and NRF1 (Figure 5) and inhibition of mitophagy (Figure 5c), possibly due to inhibition of the NAD^+ and SIRT-1-dependent mitophagy activators PINK1 and Parkin [35], [36], [37] in the GSD1a patients' cells. These results correlate with the reduced expression of SIRT1 in the livers of *L.G6pc*$^{-/-}$ mice [38]. Moreover, as in our GSD1a human fibroblasts, downregulation of *G6PC1* in *G6PC1* KD AML cells was associated with mitochondrial depolarization (decreased TMRE fluorescence), and reduced TFAM and NRF-1 dependent mitochondrial biogenesis. PGC1α levels were also reduced in livers of *L.G6pc*$^{-/-}$ KO mice *in vivo* [19].

Impairment of autophagy was previously found in hepatic cells, and in murine and canine models of GSD1a, where stimulation of the anti-autophagic mTOR and inhibition of the pro-autophagic AMPK pathways were recorded [22].

We have found preliminary indications for an epigenetic signature in GSD1a cells demonstrated by the high AcK27 histone 3 levels (Figure 4f) and the global pattern of non-methylated regions of genomic DNA (Supplementary Figure 4) as compared to HC. The effect of GHF201 treatment in GSD1a cells reverses the levels of most of these disease markers including glycogen, suggesting that the known glycogen-reducing agent helps improve the overall GSD1a phenotype in cells (Figure 6b) while also being a systemic therapy as suggested by its ameliorating effects in a GSD1a mouse model (Figure 7). These drug effects strongly support the specificity of the GSD1a phenotype in the patients' primary fibroblast. In contrast to GSD1a cells, APBD fibroblasts express the GBE pathogenic mutation linked to the cellular accumulation of polyglucosan that is significantly reduced by GHF201 in the cells [13].

Moreover, the liver functions that were improved by GHF201 treatment in *L.G6pc*$^{-/-}$ mice corroborate the relevance of the compound effect on the disease phenotype of patients' GSD1a fibroblasts, which are not the directly affected tissue by the disease as the liver cells.

These results strongly link the metabolic disease status of the cells and the aberrant transcriptional regulation found in GSD1a fibroblasts which might suggest an epigenetic change in the chromatin. In relevance to establishing the connection between metabolism and epigenetics, several studies showed that this connection is integral to the expression of gluconeogenic and glycogenolytic genes via decreased levels of the histone modifying enzyme LSD1 in HepG2 cells [39]. Moreover, Sirt1 was displayed as a key mechanistic factor for the impaired hepatic autophagy phenotype described in *L.G6pc*$^{-/-}$ mice [38], similar to the one described here in afflicted GSD1a patients fibroblasts.

The meaning and importance of a cell memory mechanism in somatic cells like GSD1a skin fibroblasts that allegedly do not comprise the tissue affected by the disease is that these cells remember the disease and respond to external conditions and therapeutic cues in the same way as primary affected cells, such as liver cells. This behavior implies that cells in the entire organism are affected by the disease and not only the cells expressing the mutated gene, even though the latter are responsible to initiate the effect on the function of the entire organism. Intriguingly, this new concept might lead to a full revision of thoughts on the efficacy and future of tissue-targeted gene therapies like those being developed for GSD1a [40], [41]. We think that the memory imprinting effect described here in GSD1a patients' fibroblasts should be considered in the development and evaluation of the long-term efficacy of targeted gene therapies for this devastating disease. In extrapolation, we anticipate that, being based solely on the Sanger sequence of affected genes, gene therapy will not be able to erase the disease signature from fibroblasts or other tissues which are not genetically implicated in the disease, but which might contribute to its pathology by their environmental imprinting. For GSD1a, it is probable that potential GSD-curing small molecules such as GHF201 could complement putative gene therapy by supplementing the genetic treatment with an active glycogen-reducing effect to reverse the established pathology in peripheral patients' tissues.

Methods

Table 1

Cell Type	Cell id	Age	Gender
GSD1A	0762	5	Male
GSD1A	75858	19	Male
GSD1A	361	15	Female
GSD1A	6894	25	Male
GSD1A	63852	14	Female
HC	GM00498	3	Male
HC	GM00038	9	Female
HC	GM07522	19	Female
HC	GM00499	8	Male

HC	GM09503	10	Male
HC	GM17507	16	Male
HC	GM03377	19	Male
HC	GM05400	6 YR	Male

Table 2

Antibody	Company	Dilution	Method
Rb- NRF1 (ab34682)	Abcam	1:1000	WB
Rb-TFAM (D5C8)	Cell Signaling Technology	1:1000	WB
Rb- COXIV (3E11)	Cell Signaling Technology	1:1000	WB

Goat-PGC1α (ab106814)	Abcam	1:50	IF
Rb-TFEB(D207D)	Cell Signaling Technology	1:100	IF
Rb-P62(109012)	Abcam	1:150	IF
Rb-LC3(2775S)	Cell Signaling Technology	1:1000	WB
Rb- Sirt-1(ab189494)	Abcam	1:100	IF
Donkey anti-rabbit Alexa Fluor 488 conjugated	BETHYL	1:1000	IF
Donkey anti-goat Alexa Fluor 488 conjugated	Thermo	1:1000	IF

HRP-conjugated donkey anti-rabbit	Abcam	1:10000	WB
Histone H3K27ac antibody (pAb) Rabbit anti immunogenic peptide	Active Motif	1:200	IF

Reagents: Chemicals and reagents were purchased from Merck-Sigma-Aldrich or as otherwise stated.

Cell culture. Primary Skin fibroblasts were isolated from skin biopsies of 5 GSD1A patients (age 5-25). Informed written consent to participate in the study was obtained from all individuals or their parents in the case of minors. The study was approved by the ethics committee of the Institutional Review Board of the Sheba Medical Center (5722-18-SMS). Age and gender matched healthy controls were purchased from Coriell Institute (New Jersey, USA) (see table 1). Primary fibroblasts were then expanded in culture media DMEM supplemented with 1% MEM Sodium Pyruvate, 1% PSA (Biological industries, Israel), 10% heat inactivated FBS, and 1% NEAA in polystyrene plastic 75-cm2 culture flasks (Corning, NY) at 37°C with 5% CO2. Cells passages and expansion of human skin fibroblasts were performed when cells were at 80-100% confluency. Cells passaging and re-plating was accomplished using 0.25% Trypsin-EDTA (Biological industries, Israel) for 2 minutes, followed by addition of twice the volume of a complete culture media to neutralize the enzyme. Cells were subsequently centrifuged at 1200 rpm for 5 minutes before their pellets being resuspended in 1 ml medium for cell counting using TC10 automated cell counter (BioRad USA) before re-plating. All experiments were performed between passages 8– 16.

Live Imaging. GSD1A and HC skin fibroblasts were seeded at 1,400 cells per well and cultured in specialized microscopy□grade 96□well plates (Cellvis P96-1.5H-N). Following 24 h in complete medium (DMEM with glucose,10% FBS, PSA, NEAA and sodium pyruvate), cells were washed to remove traces of serum and starvation medium (DMEM serum free, glucose and pyruvate free, with PSA) was applied for 24 and 48 h or for 48 h followed by 24 h with complete medium containing glucose (72 h). Before imaging, the cells at the end of their respective time points were washed and a mix of live fluorescent dyes in HBSS was added to each well for 20 min at 37°C in a 5% CO_2 incubator. The mix dilution from stock solutions is the following: 1.6mM Hoechst 33342, 0.1 mM LysoTracker Deep Red,

0.05 mM TMRE and 0.4 mM calcein-AM Green. Dilution factors are as follows: 1:2000, 1:1000, 1:500, 1:500 Respectively. Following the incubation, cells were washed with HBSS, and plates were transferred to an Operetta G1 system for image acquisition at 20× magnification under environmental control conditions at 37°C and 5% CO_2. All the assay parameters (including the acquisition exposure times, objective, and the analysis parameters) were kept constant for all assay repetitions. Images were analyzed by a customized image analysis protocol designed for the experiment using Harmony image analysis software. Downstream analysis was inspired by Caicedo et al. [42], that included quality control assessment for each plate, well removal based on extreme values, removal of outlier wells, feature selection by backward feature elimination and normalization to HC levels prior to statistics. Multivariate analysis was performed in Python. For further information see Data Analysis below and supplementary data 2.

Mitochondrial activity assays. Mitochondrial respiration (OCR and ECAR) was quantified in real-time using the Seahorse extracellular XFe96 flux analyzer (Agilent) for cells from primary skin fibroblast. Cells were plated in XFe96 cell culture plates at a density of (40000 cells/well). Cells were washed in assay media (XF Base media (Agilent) with glucose (10 mM), sodium pyruvate (1 mM) and L-glutamine (2 mM) (Gibco), pH 7.4 at 37 °C). OCR and ECAR were measured during a Seahorse Mito Stress assay (Agilent), with the addition of oligomycin (1.5µM), carbonyl cyanide 4-(trifluoromethoxy) phenylhydrazone (FCCP; 2 µM) and antimycin A and rotenone (0.5 µM each)). For ATP fluxes from glycolysis and oxidative phosphorylation estimation, Agilent's Seahorse Real-Time ATP assay kit was used. Cells were seeded and serum/glucose-starved for 48 h and the full medium was replenished for 24 h without (UT) or with (chronic) 50 µM GHF201. Acute, 50 µM GHF201 was added to an assay for 20 min after 24 h of serum/glucose replenishment. The assay employs a sequential injection of Oligomycin and Rotenone/Antimycin A. Agilent Seahorse XF Glycolysis Stress Test was performed using an XFe96 analyzer. Cells were treated with 50 µM GHF201. The assay consists of the subsequent addition of glucose, oligomycin and 2-DG and measuring the key parameters of the glycolytic function.

Immunofluorescence. 1800 cells per well were plated in 96 well plates (Cellvis P96-1.5H-N), cultured overnight for attachment and treated with 50uM GHF201 for 72 hs; 48 hs in starvation medium, followed by the replacements with complete medium for 24 h as described above. Cells were fixed in 4% paraformaldehyde in PBS, washed three times in PBS, permeabilized in 0.1% Triton X-100 in PBS for 5 min and blocked-in blocking buffer (5% FBS & 2% BSA in PBS) for 1 h. Cells were then incubated with primary antibodies (see Table 2) overnight, followed by three washes in 0.05% Triton X-100 in PBS and incubation with secondary antibodies and counterstained with 1.6mM Hoechst 33342 (1:1000) and 0.02 mM phalloidin Atto 565 (1:400) for 1 h. Cells were washed three times in PBS. Images were acquired with 20x magnification using the Operetta High content imaging system. The experiment was repeated 3 times per primary antibody where the assay parameters (including the acquisition exposure times, objective, and the analysis parameters) were kept constant for each antibody. Images were analyzed using The Harmony image analysis software using a customized image analysis protocol and quantified for intensity levels of each antibody. Each plate was normalized using the max intensity levels, then the

similar plates were combined, normalized to HC levels to perform statistical analysis. Outlier value detection was used to remove outlier wells using the Prism Route method (Q=10%).

Lysosomal pH ratiometric measuring. Ratiometric analysis of Lysosensor dye labeling for lysosomal pH was analyzed using ratiomeric fluorimetry by confocal microscopy analysis as described previously [13].

Immunoblotting. Healthy and GSD1A cells were cultured, seeded in 6 well culture plates and treated with 50uM GHF201 for 72 h as explained above. Cells were harvested and lysed in a RIPA buffer containing phosphatase inhibitor and protease inhibitor cocktails. Protein concentration was determined using a Pierce BCA protein assay kit (Thermo Fisher Scientific). Briefly, an equal amount of protein lysates was subjected to SDS-PAGE 4– 12% gradient gels and electro transferred to a nitrocellulose membrane (iBlot 2, Invitrogen). Membranes were blocked with 5% non-fat milk, incubated at 4 °C overnight with primary antibodies (see Table 1), washed, and then incubated with secondary antibodies conjugated to HRP. Proteins were then visualized by chemiluminescence reagent (Cyanagen(XLS3,0100),Thermo Fisher(34580)) using Amersham Imager 600 (GE Healthcare) and band densitometry was measured using FIJI software. Experiments were repeated independently three times.

Autophagy Flux calculation: Autophagy Flux was calculated using the formula below using the data acquired from different blots as shown in Fig3, Vinblastine (Caymen,11762) was applied in 50uM concentration 2 hours prior to protein extraction.

$$J = \frac{LC3ii/LC3i(\text{ with vinblastine})}{LC3ii/LC3i(\text{ without vinblastine}}$$

PAS. For PAS staining of glycogen, GSD1A and HC skin fibroblasts were seeded at 1,400 cells per well and cultured in microscopy□grade 96□well plates (Cellvis P96-1.5H-N) for 24 h in complete medium, then fixed and permeabilized with 0.1% Triton X□100 as described above. PAS staining was performed using Merck PAS assay kit (cat.101646), in a similar way but without amylase treatment as previously described by us [12]. The PAS-stained cells were imaged using InCell2200 (GE Healthcare, U.K.) with Texas red channel filters. Image analysis for cellular PAS staining was performed using In Carta image analysis software, total intensity was measured and compared between groups. The experiment was repeated independently three times.

NAD/NADH measurements. GSD1A and HC skin fibroblasts were seeded at a density of 10,000/well in a 384 white-walled tissue culture plate (greiner bio-one -E21123EA) (n = 5 technical replicates). Cells were treated with 50uM of GHF201 for 48 h without sugar and serum, followed by replenishment of sugar and serum for 24 h with 50uM of GHF201. The final volume per well should be 50ul. On the day of the experiment the plate was equilibrated at room temperature for 5 minutes. 50ul of NAD/NADH-Glo™ Detection Reagent (Promega) was added to each well. Plates were Gently and briefly shaken to mix lyse cells. The cells were incubated with NAD/NADH-Glo™ Detection Reagent for 30–60 minutes at room

temperature. The luminescence was recorded using a luminometer. respectively. In parallel, the same batch of cells was also subjected to dynamic Incucyte analysis of cell confluency and cell death over time.

Global unmodified CpG pattern analysis. Global unmodified CpG islands were characterized using the methodology described previously [43],[44], [45].

DNA construct and expression for the mitophagy assay. A plasmid encoding mCherry, GFP and residues 101 to 152 of human FIS1 (mCherry-GFP-FIS1 101 to 152) was obtained from the University of Dundee (MRC-PPU reagents, DU40799) [27]. cDNA for mCherry, GFP and residues 101–152 of human FIS1 were cloned into a pBABE.hygro vector. The construct was co-transfected into 293FT cells with GAG/POL gpt and VSV-G expression plasmids. For retrovirus production, calcium phosphate precipitation method was used. Supernatant containing retrovirus was collected 48 h after transfection and was filtered using a 0.45 mm filter. HC and GSD1a fibroblast cells were infected with filtered viral supernatant containing 8 mg/ml polybrene. 2 days after the infection the cells were allowed to grow and the experiment was performed as described.

Mitophagy assay. Cells stably expressing mCherry-GFP-FIS1-leading sequence [OK1] [46], were plated on a 96 well plate and treated with GHF201 for 24 hours. Next day, cells were treated with 4 µM FCCP for 20 minutes. Cells were washed with phosphate-buffered saline, fixed with 4% paraformaldehyde, washed thrice, incubated for 10 min with Hoechst (to stain the nuclei), washed thrice with phosphate-buffered saline and plates were transferred to an Operetta G1 system for image acquisition at 20× magnification in 37°C in a 5% CO2. Images were analyzed using the Harmony image analysis software using a customized image analysis protocol.

***In vivo* experiments**

Liver G6pc KO was induced in L-G6PC$^{-/-}$ mice using a CRE recombinase fused to a mutated ligand-binding domain of the estrogen receptor, activated by tamoxifen treatment, as described in [47]. Briefly, a group of 5 male mice per arm (6–7-week-old) were treated by 0.2 mg/day of tamoxifen. One month after *G6pc1* deletion, ND-GHF-201 was administered daily *per os* at 70 mg/mL. After 4 weeks, mice were starved for 6 h, euthanized by cervical dislocation and liver and blood samples were collected for further analyses. Liver glucose-s-phosphate, glycogen and glucose and blood glucose were determined as previously described [47]. Mice were housed in the animal facility of Lyon 1 University (Animaleries Lyon Est Conventionnelle et SPF) in controlled temperature (22 °C) conditions, with a 12-h light-12-h dark cycle and free access to water and standard rodent chow. Fasting was conducted with free access to water. All procedures were performed in accordance with the principles and guidelines established by the European Convention for the protection of Laboratory Animals and were approved by the local animal ethics committee and the French Ministry of National Education, Higher Education and Research (Apafis Permit #30629).

Statistics. Generally, in all experiments n was between 3 – 5 for the GSD1a treated and untreated groups and between 3-6 for the HC group.

All statistical tests were performed in GraphPad Prism 9, unless otherwise mentioned a 2 tailed unpaired t test was performed to compare groups.

P values were characterized as follows: 0.0001 - ****,0.001- *** ,0.01 - **,0.1- *

Data analysis. Generally, all data processing stages in all experiments were performed using python 3 and R Studio.

High quality image-based analysis is important and effective in biological data [48], [49]. Specifically, in this work, prime Image analysis was customized for each experiment using the Harmony image-analysis software. For fig 1 analysis included quality control per plate, well removal based on cell count, Outlier identification [50] to remove wells with extreme values, feature selection using backward feature elimination to remove correlated features and to select equal number of features per organelle to allow an unbiased approach for the multivariate analysis. Finally, multivariate analysis highlighting ideal dimension reduction algorithms that were chosen based on their overall fit to the data [51] for fig. 5 features were averaged and normalized to the same scale by standardization to allow multi-level feature data to be integrated. Correlation analysis was performed by python using pearson test [52]. Network analysis and K-Means analysis [53] were performed using the R studio software (vs 4.2.2). Visualization for several plots created through the MS were generated using Plotly [54].

Data and code Availability

scripts for the main analysis sequences described could be found here -

https://github.com/Urisprecher/GSD1a_MS_2023

Additional code and data are available upon request.

Acknowledgments

We would like to thank the following people: Dr. Yuval Ebenstein and Dr. Rachel Zamostiano, Tel Aviv University for their advice and technical support; Yuval Raviv for the initial contribution to the project; Roi Ronen for the comments and advice on the algorithms used; and Dr. Ido Goldstein from the Hebrew University of Jerusalem for the Histone H3K27ac antibody. We thank Dr. Oded Rechavi for the useful comments to this manuscript. This work was funded by the Krigsner Foundation. This work is dedicated to the memory of David Krigsner Zindeluk (z"l).

Author contributions

US, JD, KM, and CMA designed and performed experiments; SA, GM, and FR designed experiments and critically reviewed the manuscript; YA contributed clinical samples and reviewed the manuscript; OK and MW designed, supervised experiments, and wrote the manuscript.

Conflict of interest

The authors claim that they don’t have any conflict of interest.

OK and MW who are part of the investigators and authors of this manuscript serve as consultants to GHF-Golden Heart Flower Ltd. All the IP rights in the inventions described in this manuscript were licensed to GHF.

Legends GSD1A manuscript 2023

FIG1 – GSD1a fibroblasts HCA phenotyping

a. Representative images of HC fibroblasts(left) and GSD1a fibroblasts(right), showcasing the organelles labeled in this experiment, Hoechst 33342 for nucleus (Blue), calcein-AM for cytoplasm (Green), TMRE for active mitochondria (Yellow) and lysotracker for lysosomes (Red).

b. Heatmap representing 6 features for each organelle, each row presenting normalized average values for HC and GSD1a samples in each time condition. The different feature names shown for each label are numbered 1 to 6 for simplification. Original names are mentioned in Supplementary table 1.

c. PCA plot showing GSD1a samples averaged from each time condition (Red gradient), and HC samples averaged from each time condition (Blue gradient).

d. LDA plot, showing all GSD1a samples grouped from all time conditions (Red) compared to all HC samples grouped from all time conditions (Blue).

FIG2 - Metabolic profiling of GSD1a and HC samples treated with GHF201

a. Representative quantification of real-time cellular oxygen consumption rates (OCR) of GSD1a and HC fibroblasts treated with 50 µM GHF201. Dash line indicate the addition of mitochondrial inhibitors (oligomycin; FCCP; antimycin A/rotenone) for assessment of mitochondrial respiration.

b-g. Changes in OCR identified from HC and GSD1a samples. (b – basal respiration, c - maximal respiration, d - ATP production, e - spare respiratory capacity, f - proton leak and g - non-mitochondrial respiration).

h. Representative quantification of real-time ATP production rates by glycolysis and OXPHOS in GSD1a and HC samples treated with 50 µM GHF201.

i. Quantification of extracellular acidification rate (ECAR) across time is measured from HC and GSD1a samples treated with 50 µM GHF201. Dash line indicate the. Sequential compound injections (Glucose, Oligomycin and 2-DG).

j-k. Bar graphs representing the measurements of glycolysis, glycolytic capacity from (i).

FIG3 – Lysosomal profiling in GSD1a and HC sample treated with GHF201

a. Lysosomal pH measurement in GSD1a and HC fibroblasts by flow cytometry, using the lysosomal ratiometric pH sensor Lysosensor, Left Hand panel shows representative examples summarized as bar graphs in the right-hand panel.

b. Representative blot, presenting Autophagic flux, determined by the extent of lysosomal inhibitor (Vinblastine)-dependent increase in the ratio of lipidated to non-lipidated LC3 (LC3II/LC3I), Shown are representative immunoblots(left) and densitometric quantifications comparing Autophagic flux levels between HC(BLUE), GSD1a(RED) and GSD1a treated (GREEN) fibroblasts.

c. Scatter plots representing p62 intensity normalized to HC levels. Comparing intensity levels between HC(BLUE), GSD1a(RED) and GSD1a treated (GREEN) fibroblasts.

d. Scatter plots representing TFEB intensity normalized to HC levels. Comparing intensity levels between HC(BLUE), GSD1a(RED) and GSD1a treated (GREEN) fibroblasts.

FIG4 – Identification of potential mechanism behind the phenotype in GSD1a samples.

a. Scatter plots representing p-AMPK divided by total-AMPK intensity normalized to HC levels. Comparing intensity levels between HC(BLUE), GSD1a(RED) and GSD1a treated (GREEN) fibroblasts.

b-d. GHF201 increases the NAD^+/NADH ratio and viability in Gsd1a fibroblasts under basal and ATPdemand conditions. Left panel, NAD^+/NADH ratio in Gsd1a fibroblasts under the indicated treatments was determined by the Promega kit. ATP demand was imposed by gramicidin, which increases ATP consumption and the ADP/ATP ratio, and consequently depolarizes mitochondria

and increases the NAD^+/NADH as compared to untreated cells ($p<0.1$). NAD^+/NADH ratio was also increased by GHF201 and by the gramicidin/GHF201 combination as compared to untreated cells ($p<0.1$ and $p<0.02$, respectively). The mitochondria hyperpolarizing agent Oligomycin A reduced NAD^+/NADH as compared to untreated cells ($p<0.04$). NAD^+/NADH ratios were inversely correlated with cytotoxicity over time, measured by Cytotox red (middle panel), and positively correlated with cell confluence over time (right panel).

e. Scatter plots representing SIRT1 intensity normalized to HC levels. comparing intensity levels between HC(BLUE), GSD1a(RED) and GSD1a treated (GREEN) fibroblasts.

f. Histone H3K27ac acetylation (green) in the nuclei (blue) of GHF201 treated and untreated GSD1a and HC fibroblasts. Shown are representative nuclei images and quantification of green fluorescence in single nuclei.

FIG5 – Assessment of mitochondrial function

a. Scatter plots representing PGC1α intensity normalized to HC levels. comparing intensity levels between HC(BLUE), GSD1a(RED) and GSD1a treated (GREEN) fibroblasts.

b. Representative blot, presenting mitochondrial biogenesis and activity markers, shown are representative immunoblots(up) and densitometric quantifications comparing levels between HC(BLUE), GSD1a(RED) and GSD1a treated (GREEN) fibroblasts.

c. Scatter plots representing the comparisons between HC(BLUE), GSD1a(RED) and GSD1a treated (GREEN) fibroblasts all treated with FCCP and quantified for the ratio between mCherry intensity levels and the total intensity of GFP and mCherry combined. The results are represented by images of all three groups shown on the right.

FIG6 - integrated analysis of HC, GSD1a and GSD1a treated samples.

a. Correlation bubble plot representing a Pearson correlation analysis performed on GSD1a and HC samples, measuring the interaction between selected features from the HCA experiment and several markers assessed here. Features are categorized as HCA or biochemical-analysis based. The Radius and color of the circles reflects the correlation coefficient value; significant correlations are noted by asterisks.

b. K-means clustering plot calculated by K-means algorithm(k=3) using data from GSD1a, Treated GSD1a and HC samples integrating features obtained from the biochemical experiments. The circle of each cluster reflects a 95% confidence interval.

c. Network analysis visualization presenting the interaction between key markers in GSD1a samples(left) and treated GSD1a samples(right). The node color indicates the marker pathway, node size represents the measured value of the marker. Edge weight indicates the strength of the marker's interaction by the literature.

FIG7 – Evaluation of GHF201 *In vivo* by using a GSD1a mouse model

a. Schematic representation of the in-vivo pipeline performed on GSD1a mouse models to test GHF201.

b-f. Bar plots showcasing the differences in Glucose-6-phosphatase, Glucose, glycemic index, Glycogen content and liver weights between LG6PC -/- vehicle and LG6PC -/- GHF201 mouse.

Supplementary FIG1 – Feature contributing to LD1 explained variance

The top ten contributing features to the variance explained by the first component of the LDA, including TMRE, Lysotracker, calcein-AM and Hoechst features. (Features full names in supplementary table 1).

Supplementary FIG2 – Effect of GHF201 on GSD1a fibroblasts by PAS assay

Representative images of a PAS assay experiment on GSD1a fibroblasts and GSD1a fibroblasts treated with GHF201 (left).

In addition, scatter plots representing Glycogen intensity, comparing intensity levels between GSD1a(RED) and GSD1a treated (GREEN) fibroblasts.

Supplementary FIG3 – Representative images of Immunofluorescence markers

A panel of images obtained from the Immunofluorescence experiments performed in this work, showing representative images for HC, GSD1a and GSD1a treated fibroblasts from left to right. Markers are ordered from top to bottom: Sirt1, Tfeb, PGC1α, AMPK, p-AMPK. P62.

Supplementary FIG4 – Global unmethylated regions comparison between HC and GSD1a fibroblasts

Slides consisting of DNA from HC and GSD1a fibroblasts, selectively marked by EvaGreen(DNA dye- Up) and TAMRA(unmethylated CpG regions dyw- Down).

On the bottom a quantification of the above mentioned analysis comparing unmethylated CpG regions levels normalized to total DNA between HC and GSD1a fibroblasts.

References

1. Raza, M., Arif, F., Giyanwani, P. R., Azizullah, S. & Kumari, S. Dietary Therapy for Von Gierke's Disease: A Case Report. *Cureus* **9**, (2017).

2. Kishnani, P. S. *et al.* Diagnosis and management of glycogen storage disease type I: a practice guideline of the American College of Medical Genetics and Genomics. *Genet. Med.* **16**, 1–29 (2014).

3. Chou, J. Y., Kim, G. Y. & Cho, J. H. Recent development and gene therapy for glycogen storage disease type Ia. *Liver Res.* **1**, 174–180 (2017).

4. Shieh, J. J. *et al.* The molecular basis of glycogen storage disease type 1a: structure and function analysis of mutations in glucose-6-phosphatase. *J. Biol. Chem.* **277**, 5047–5053 (2002).

5. Rajas, F., Bruni, N., Montano, S., Zitoun, C. & Mithieux, G. The glucose-6 phosphatase gene is expressed in human and rat small intestine: Regulation of expression in fasted and diabetic rats. *Gastroenterology* **117**, 132–139 (1999).

6. Molares-vila, A., Corbalán-rivas, A., Carnero-gregorio, M., González-cespón, J. L. & Rodríguez-cerdeira, C. Biomarkers in Glycogen Storage Diseases: An Update. *Int. J. Mol. Sci.* **22**, 4381 (2021).

7. Ellingwood, S. S. & Cheng, A. Biochemical and clinical aspects of glycogen storage diseases. *J. Endocrinol.* **238**, R131–R141 (2018).

8. Parikh, N. S. & Ahlawat, R. Glycogen Storage Disease Type I. *StatPearls* (2022).

9. Oster, Y., Wexler, I. D., Heyman, S. N. & Fried, E. Recoverable, Record-High Lactic Acidosis in a Patient with Glycogen Storage Disease Type 1: A Mixed Type A and Type B Lactate Disorder. *Case Rep. Med.* **2016**, (2016).

10. Mathis, T. *et al.* Untargeted plasma metabolomics identifies broad metabolic perturbations in glycogen storage disease type I. *J. Inherit. Metab. Dis.* **45**, 235–247 (2022).

11. Bali, D. S., El-Gharbawy, A., Austin, S., Pendyal, S. & Kishnani, P. S. Glycogen Storage Disease Type I. *GeneReviews*® (2021).

12. Solmesky, L. J. *et al.* A novel image-based high-throughput screening assay discovers therapeutic candidates for adult polyglucosan body disease. *Biochem. J.* **474**, 3403–3420 (2017).

13. Kakhlon, O. *et al.* Alleviation of a polyglucosan storage disorder by enhancement of autophagic glycogen catabolism. *EMBO Mol. Med.* **13**, e14554 (2021).

14. G6PC1 (glucose-6-phosphatase catalytic subunit 1) | Gene Report | BioGPS. Available at: http://biogps.org/#goto=genereport&id=2538. (Accessed: 12th January 2023)

15. Halling, J. F. & Pilegaard, H. PGC-1α-mediated regulation of mitochondrial function and physiological implications. *Appl. Physiol. Nutr. Metab.* **45**, 927–936 (2020).

16. Napolitano, G. & Ballabio, A. TFEB at a glance. *J. Cell Sci.* **129**, 2475 (2016).

17. Zhang, T. *et al.* Heme oxygenase 1 overexpression induces immune evasion of acute myeloid leukemia against natural killer cells by inhibiting CD48. *J. Transl. Med.* **20**, 1–13 (2022).

18. Umemoto, T. *et al.* ATP citrate lyase controls hematopoietic stem cell fate and supports bone marrow regeneration. *EMBO J.* **41**, (2022).

19. Farah, B. L. *et al.* Renal endoplasmic reticulum stress is coupled to impaired autophagy in a mouse model of GSD Ia. *Mol. Genet. Metab.* **122**, 95–98 (2017).

20. Farah, B. L., Yen, P. M. & Koeberl, D. D. Links between autophagy and disorders of glycogen metabolism - Perspectives on pathogenesis and possible treatments. *Mol. Genet. Metab.* **129**, 3–12 (2020).

21. Waskowicz, L. R. *et al.* Bezafibrate induces autophagy and improves hepatic lipid metabolism in glycogen storage disease type Ia. *Hum. Mol. Genet.* **28**, 143–154 (2019).

22. Gautam, S. *et al.* The signaling pathways implicated in impairment of hepatic autophagy in glycogen storage disease type Ia. *Hum. Mol. Genet.* **29**, 834–844 (2020).

23. Hosios, A. M. & Matthew, G. V. H. The redox requirements of proliferating mammalian cells. *J. Biol. Chem.* **293**, 7490–7498 (2018).

24. Wu, Z. *et al.* Mechanisms controlling mitochondrial biogenesis and respiration through the thermogenic coactivator PGC-1. *Cell* **98**, 115–124 (1999).

25. Niu, W., Wang, H., Wang, B., Mao, X. & Du, M. Resveratrol improves muscle regeneration in obese mice through enhancing mitochondrial biogenesis. *J. Nutr. Biochem.* **98**, (2021).

26. Pejznochova, M. *et al.* Mitochondrial DNA content and expression of genes involved in mtDNA transcription, regulation and maintenance during human fetal development. *Mitochondrion* **10**, 321–329 (2010).

27. Allen, G. F. G., Toth, R., James, J. & Ganley, I. G. Loss of iron triggers PINK1/Parkin-independent mitophagy. *EMBO Rep.* **14**, 1127 (2013).

28. Koves, T. R. *et al.* Peroxisome Proliferator-activated Receptor-γ Co-activator 1α-mediated Metabolic Remodeling of Skeletal Myocytes Mimics Exercise Training and Reverses Lipid-induced Mitochondrial Inefficiency. *J. Biol. Chem.* **280**, 33588–33598 (2005).

29. Koutsifeli, P. *et al.* Glycogen-autophagy: Molecular machinery and cellular mechanisms of glycophagy. *J. Biol. Chem.* **298**, (2022).

30. Cantó, C. & Auwerx, J. PGC-1alpha, SIRT1 and AMPK, an energy sensing network that controls energy expenditure. *Curr. Opin. Lipidol.* **20**, 98–105 (2009).

31. Di Malta, C., Cinque, L. & Settembre, C. Transcriptional regulation of autophagy: Mechanisms and diseases. *Front. Cell Dev. Biol.* **7**, 114 (2019).

32. Mutel, E. *et al.* Targeted deletion of liver glucose-6 phosphatase mimics glycogen storage disease type 1a including development of multiple adenomas. *J. Hepatol.* **54**, 529–537 (2011).

33. Tucci, V. *et al.* Genomic Imprinting and Physiological Processes in Mammals. *Cell* **176**, 952–965 (2019).

34. Thamban, T., Agarwaal, V. & Khosla, S. Role of genomic imprinting in mammalian development. *J. Biosci.* **45**, 1–21 (2020).

35. Fang, E. F. *et al.* NAD+ Replenishment Improves Lifespan and Healthspan in Ataxia Telangiectasia Models via Mitophagy and DNA Repair. *Cell Metab.* **24**, 566–581 (2016).

36. Fang, E. F. *et al.* Mitophagy inhibits amyloid-β and tau pathology and reverses cognitive deficits in models of Alzheimer's disease. *Nat. Neurosci. 2019 223* **22**, 401–412 (2019).

37. Fang, E. F. Mitophagy and NAD+ inhibit Alzheimer disease. *Autophagy* **15**, 1112–1114 (2019).

38. Cho, J. H. *et al.* Downregulation of SIRT1 signaling underlies hepatic autophagy impairment in glycogen storage disease type Ia. *PLoS Genet.* **13**, (2017).

39. Pan, D., Mao, C. & Wang, Y. X. Suppression of gluconeogenic gene expression by LSD1-mediated histone demethylation. *PLoS One* **8**, (2013).

40. Yiu, W. H. *et al.* Complete normalization of hepatic G6PC deficiency in murine glycogen storage disease type Ia using gene therapy. *Mol. Ther.* **18**, 1076–1084 (2010).

41. Cao, J. *et al.* mRNA therapy restores euglycemia and prevents liver tumors in murine model of glycogen storage disease. *Nat. Commun. 2021 121* **12**, 1–14 (2021).

42. Caicedo, J. C. *et al.* Data-analysis strategies for image-based cell profiling. *Nat. Methods* **14**, 849–863 (2017).

43. Avraham, S. *et al.* Simultaneous global labeling (SiGL) of 5-methylcytosine and 5-hydroxymethylcytosine by DNA alkylation with a synthetic cofactor and engineered methyltransferase. *bioRxiv* 2022.10.31.513813 (2022). doi:10.1101/2022.10.31.513813

44. Margalit, S. *et al.* 5-Hydroxymethylcytosine as a clinical biomarker: Fluorescence-based assay for high-throughput epigenetic quantification in human tissues. *Int. J. cancer* **146**, 115–122 (2020).

45. Gilat, N. *et al.* Rapid Quantification of Oxidation and UV Induced DNA Damage by Repair Assisted Damage Detection-(Rapid RADD). *Anal. Chem.* **92**, 9887–9894 (2020).

46. Lim, J. A., Li, L., Kakhlon, O., Myerowitz, R. & Raben, N. Defects in calcium homeostasis and mitochondria can be reversed in Pompe disease. *Autophagy* **11**, 385 (2015).

47. Mutel, E. *et al.* Targeted deletion of liver glucose-6 phosphatase mimics glycogen storage disease type 1a including development of multiple adenomas. *J. Hepatol.* **54**, 529–537 (2011).

48. Ronen, R., Attias, Y., Schechner, Y. Y., Jaffe, J. S. & Orenstein, E. Plankton reconstruction through robust statistical optical tomography. *J. Opt. Soc. Am. A. Opt. Image Sci. Vis.* **38**, 1320 (2021).

49. Torem, N., Ronen, R., Schechner, Y. Y. & Elad, M. Towards A Most Probable Recovery in Optical Imaging. (2022). doi:10.48550/arxiv.2212.03235

50. Breunig, M. M., Kriegel, H.-P., Ng, R. T. & Sander, J. LOF: Identifying Density-Based Local Outliers.

51. Pedregosa FABIAN PEDREGOSA, F. *et al.* Scikit-learn: Machine Learning in Python Gaël Varoquaux Bertrand Thirion Vincent Dubourg Alexandre Passos PEDREGOSA, VAROQUAUX, GRAMFORT ET AL. Matthieu Perrot. *J. Mach. Learn. Res.* **12**, 2825–2830 (2011).

52. Virtanen, P. *et al.* SciPy 1.0: fundamental algorithms for scientific computing in Python. *Nat. Methods 2020 173* **17**, 261–272 (2020).

53. Kassambara, A. and Mundt, F. (2020) Factoextra Extract and Visualize the Results of Multivariate Data Analyses. R Package Version 1.0.7. - References - Scientific Research Publishing. Available at:

https://scirp.org/reference/referencespapers.aspx?referenceid=3067217. (Accessed: 27th January 2023)

54. Plotly Technologies Inc., Collaborative data science, Plotly Technologies Inc. Place of publication: Montréal, QC , 2015 URL: https://plot.ly

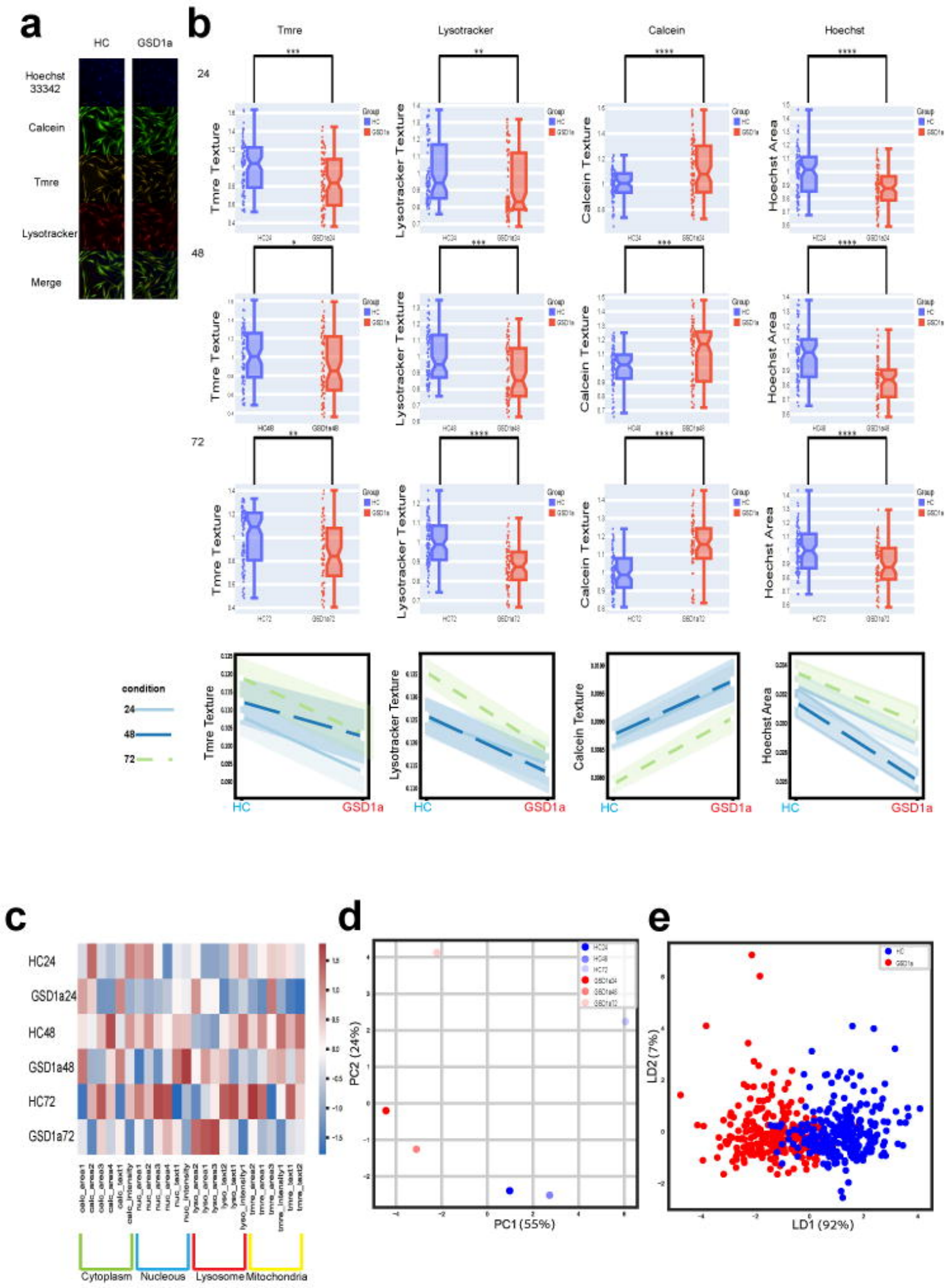
a
HC
GSD1a
Hoechst 33342
Calcein
Tmre
Lysotracker
Merge
b
Tmre
Lysotracker
Calcein
Hoechst
24
48
72
Tmre Texture
Lysotracker Texture
Calcein Texture
Hoechst Area
Group
HC
GSD1a
condition
24
48
72
HC
GSD1a
c
HC24
GSD1a24
HC48
GSD1a48
HC72
GSD1a72
calc_area1
calc_area2
calc_area3
calc_area4
calc_text1
calc_intensity
nuc_area1
nuc_area2
nuc_area3
nuc_area4
nuc_text1
nuc_intensity
lyso_area1
lyso_area2
lyso_area3
lyso_text1
lyso_text2
lyso_intensity1
tmre_area1
tmre_area2
tmre_area3
tmre_intensity1
tmre_text1
tmre_text2
Cytoplasm
Nucleus
Lysosome
Mitochondria
d
HC24
HC48
HC72
GSD1a24
GSD1a48
GSD1a72
PC1 (55%)
PC2 (24%)
e
HC
GSD1a
LD1 (92%)
LD2 (7%)

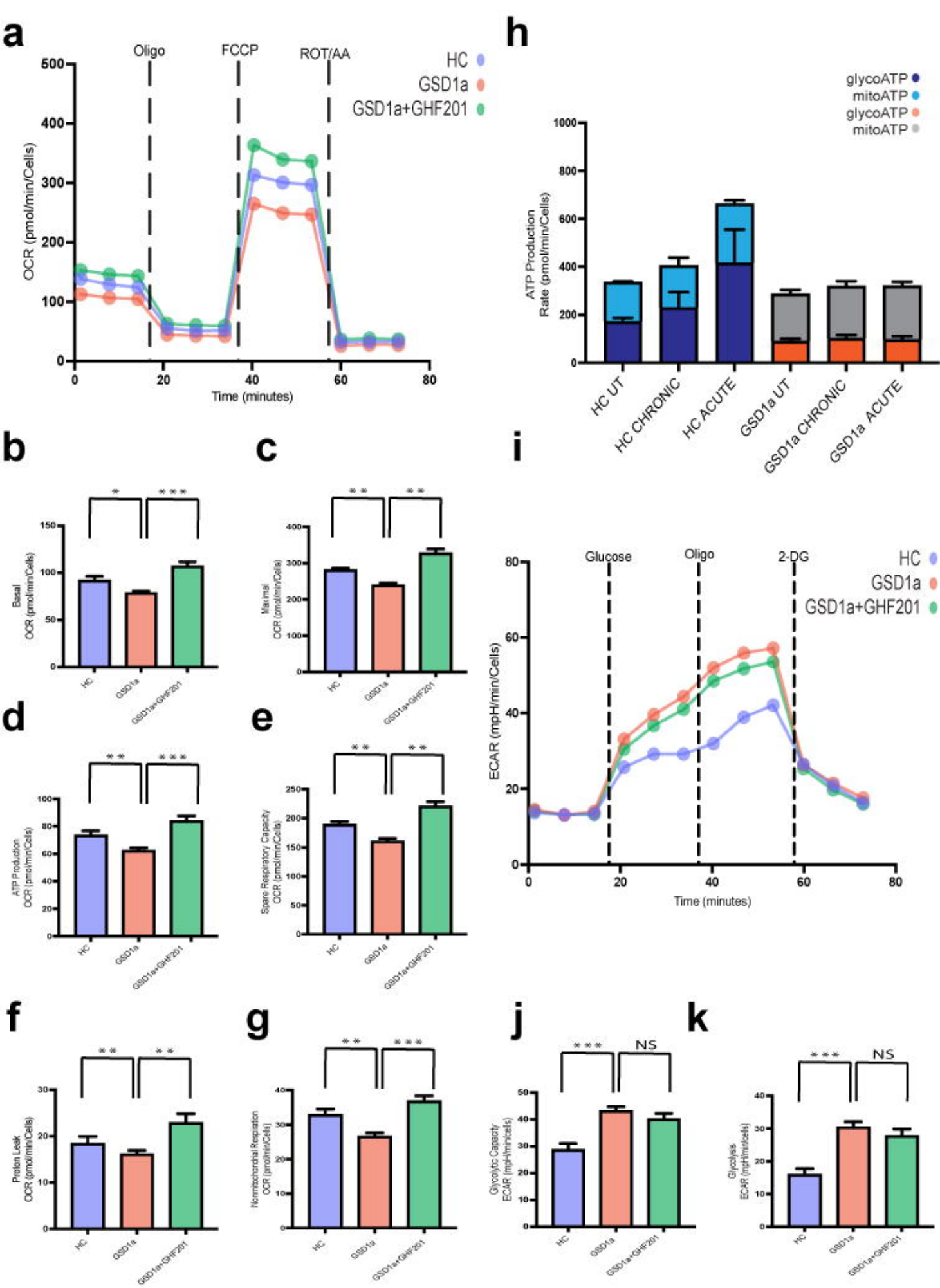
a
Oligo
FCCP
ROT/AA
HC
GSD1a
GSD1a+GHF201
OCR (pmol/min/Cells)
Time (minutes)
h
glycoATP
mitoATP
glycoATP
mitoATP
ATP Production Rate (pmol/min/Cells)
HC UT
HC CHRONIC
HC ACUTE
GSD1a UT
GSD1a CHRONIC
GSD1a ACUTE
b
Basal OCR (pmol/min/Cells)
c
Maximal OCR (pmol/min/Cells)
i
Glucose
Oligo
2-DG
HC
GSD1a
GSD1a+GHF201
ECAR (mpH/min/Cells)
Time (minutes)
d
ATP Production OCR (pmol/min/Cells)
e
Spare Respiratory Capacity OCR (pmol/min/Cells)
f
Proton Leak OCR (pmol/min/Cells)
g
Nonmitochondrial Respiration OCR (pmol/min/Cells)
j
Glycolytic Capacity ECAR (mpH/min/cells)
NS
k
Glycolysis ECAR (mpH/min/cells)
NS

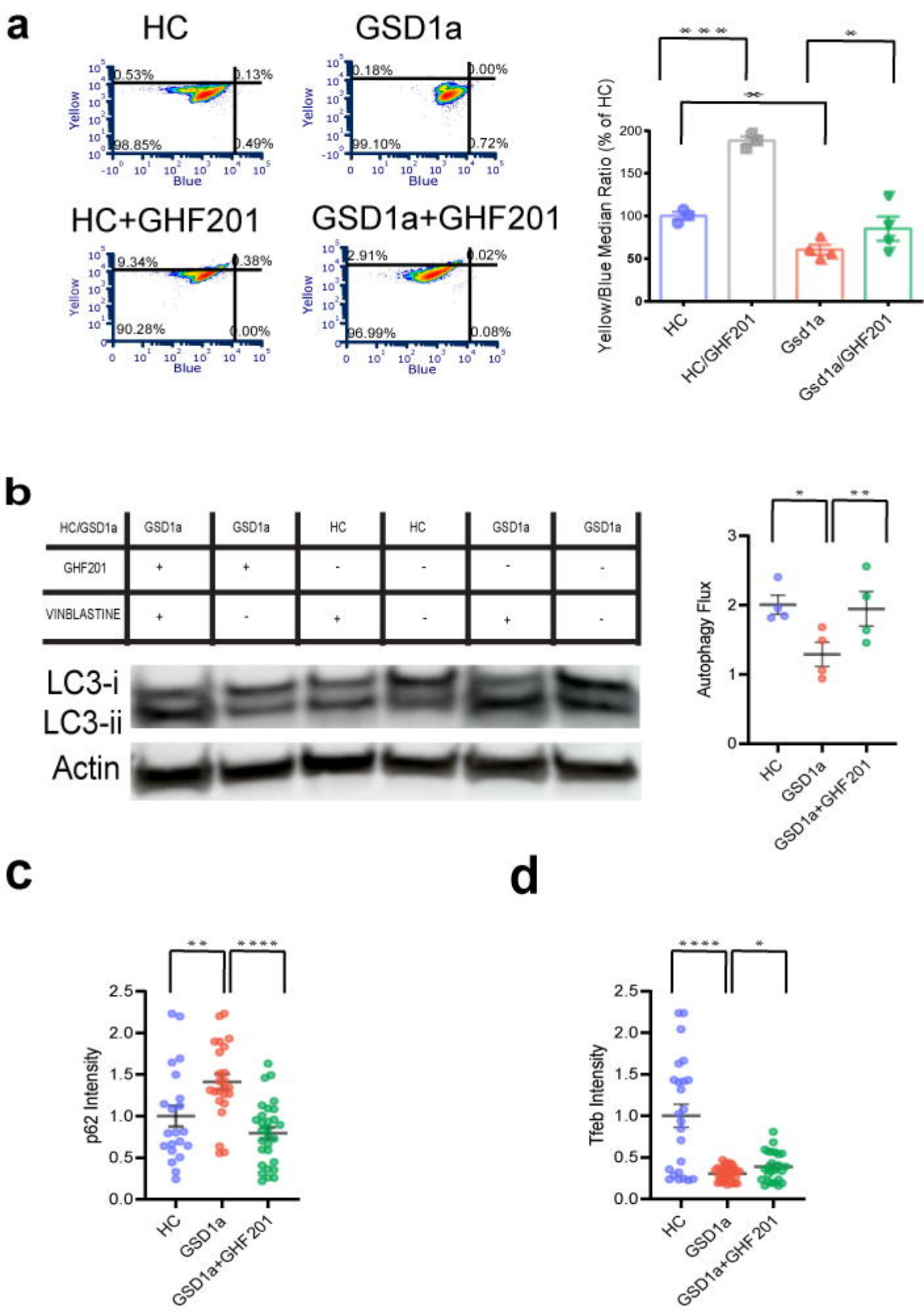
a
HC
GSD1a
HC+GHF201
GSD1a+GHF201
Yellow
Blue
0.53%
0.13%
98.85%
0.49%
0.18%
0.00%
99.10%
0.72%
9.34%
0.38%
90.28%
0.00%
2.91%
0.02%
96.99%
0.08%
Yellow/Blue Median Ratio (% of HC)
HC
HC/GHF201
Gsd1a
Gsd1a/GHF201
b
HC/GSD1a
GSD1a
GSD1a
HC
HC
GSD1a
GSD1a
GHF201
VINBLASTINE
LC3-i
LC3-ii
Actin
Autophagy Flux
HC
GSD1a
GSD1a+GHF201
c
p62 Intensity
HC
GSD1a
GSD1a+GHF201
d
Tfeb Intensity
HC
GSD1a
GSD1a+GHF201

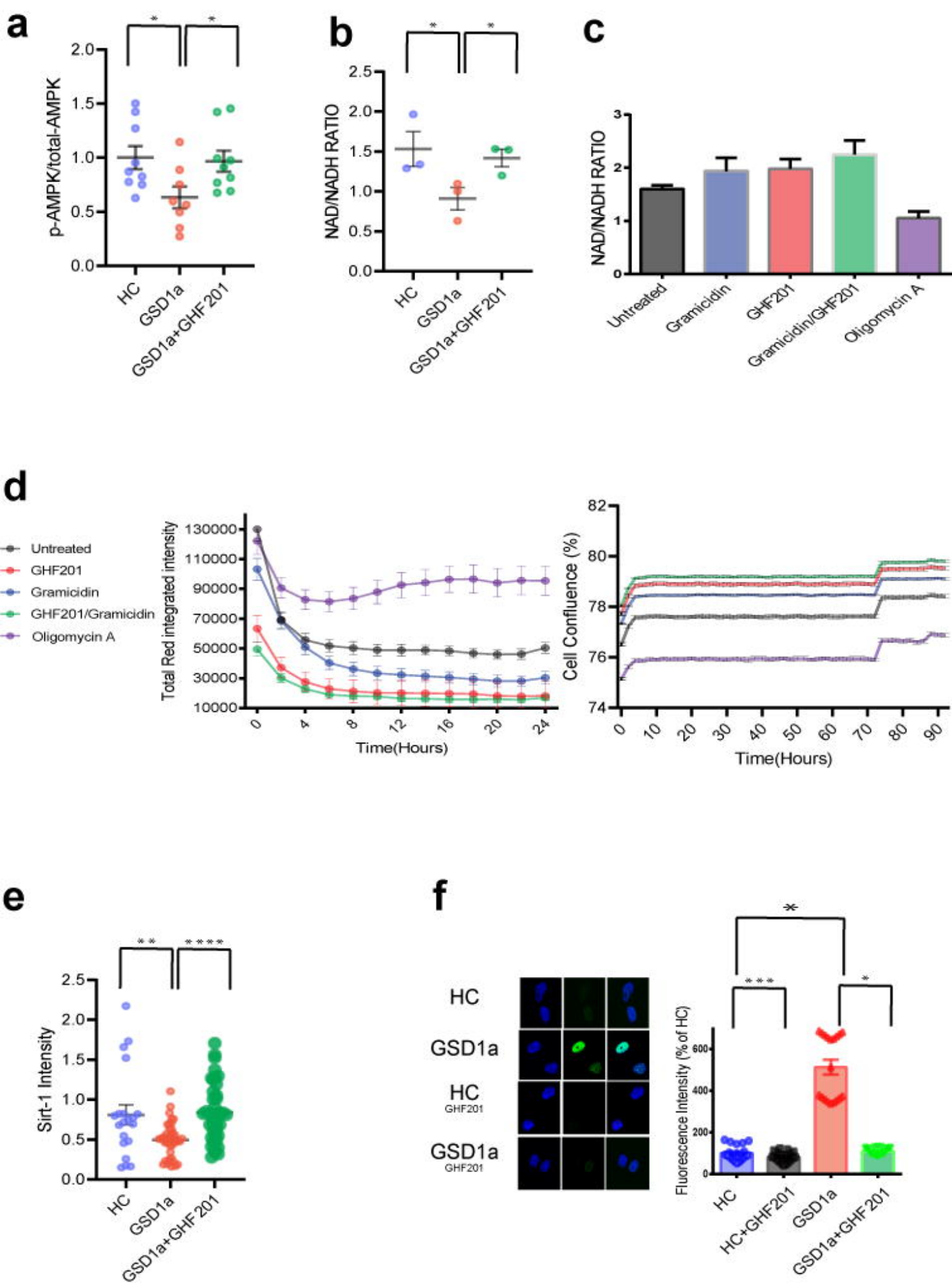
a
p-AMPK/total-AMPK
HC
GSD1a
GSD1a+GHF201
b
NAD/NADH RATIO
HC
GSD1a
GSD1a+GHF201
c
NAD/NADH RATIO
Untreated
Gramicidin
GHF201
Gramicidin/GHF201
Oligomycin A
d
Untreated
GHF201
Gramicidin
GHF201/Gramicidin
Oligomycin A
Total Red integrated intensity
Time(Hours)
Cell Confluence (%)
Time(Hours)
e
Sirt-1 Intensity
HC
GSD1a
GSD1a+GHF201
f
HC
GSD1a
HC
GHF201
GSD1a
GHF201
Fluorescence Intensity (% of HC)
HC
HC+GHF201
GSD1a
GSD1a+GHF201

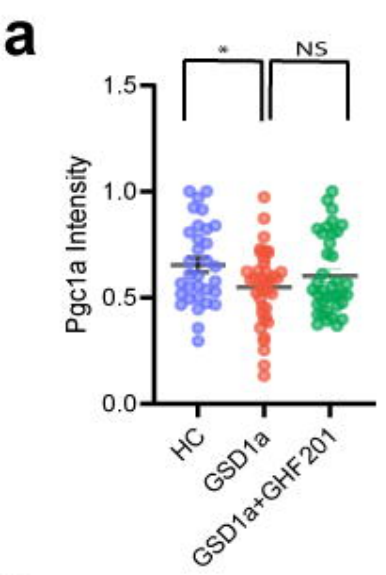
a
*
NS
Pgc1a Intensity
1.5
1.0
0.5
0.0
HC
GSD1a
GSD1a+GHF201

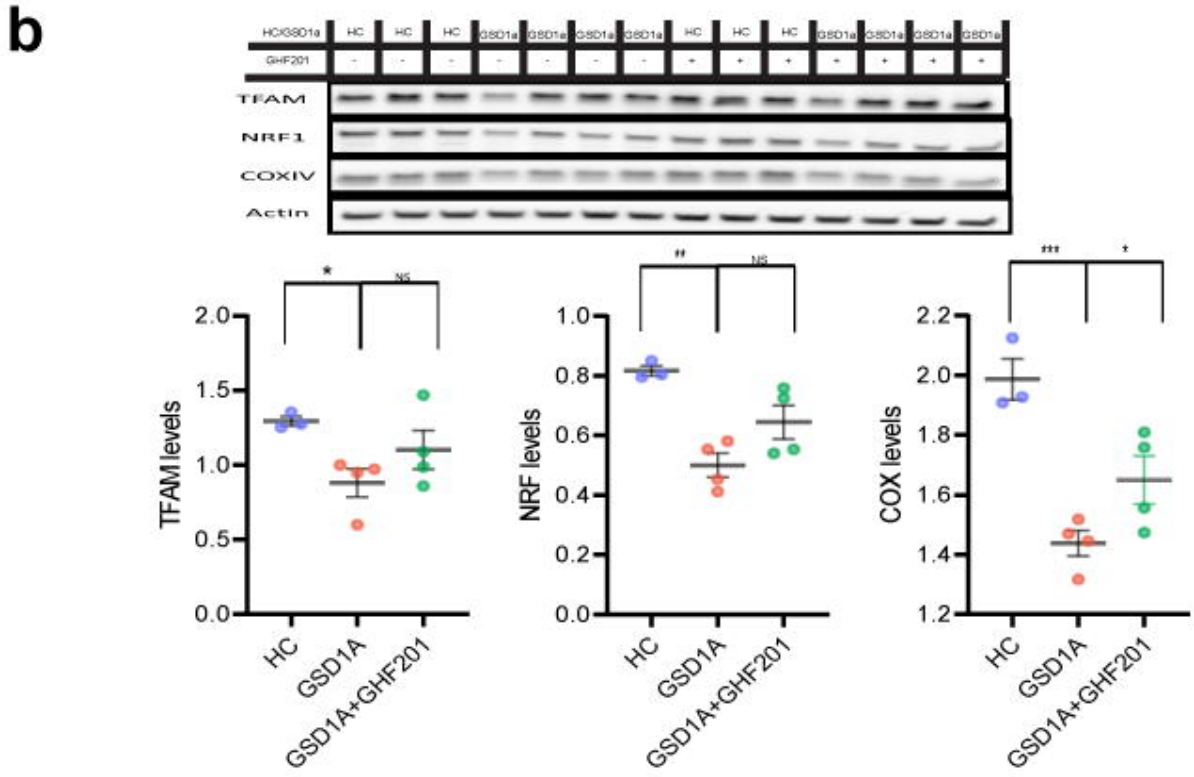
b
HC/GSD1a
GHF201
TFAM
NRF1
COXIV
Actin
TFAM levels
NRF levels
COX levels
HC
GSD1A
GSD1A+GHF201

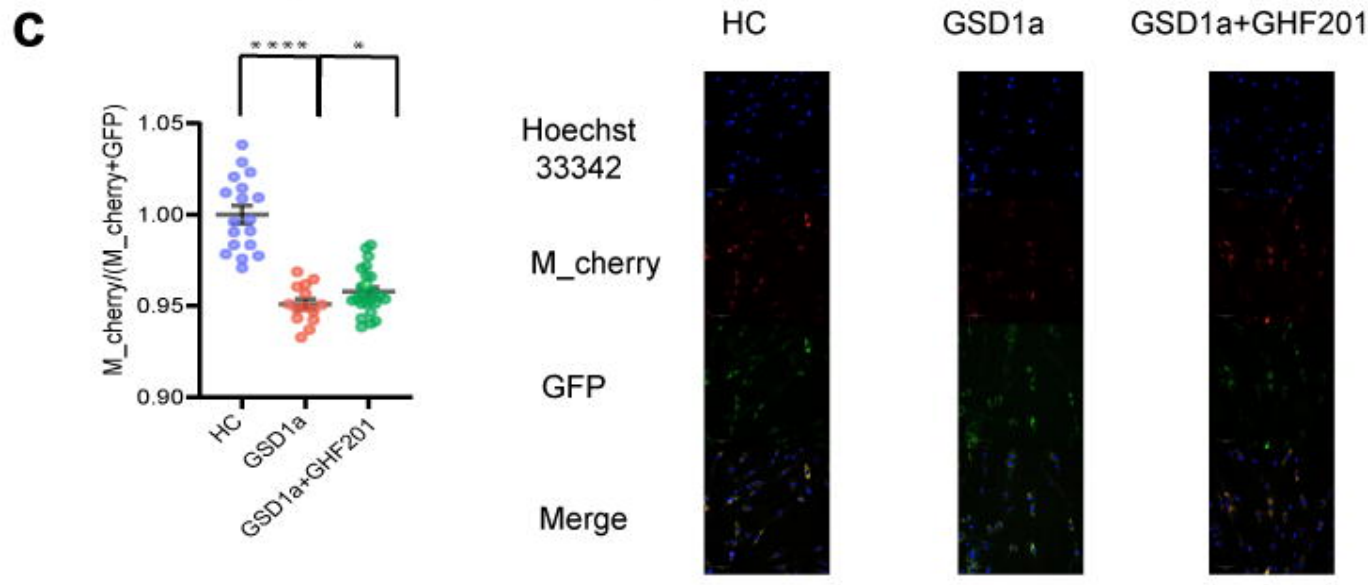
c
****
*
M_cherry/(M_cherry+GFP)
1.05
1.00
0.95
0.90
HC
GSD1a
GSD1a+GHF201
Hoechst 33342
M_cherry
GFP
Merge

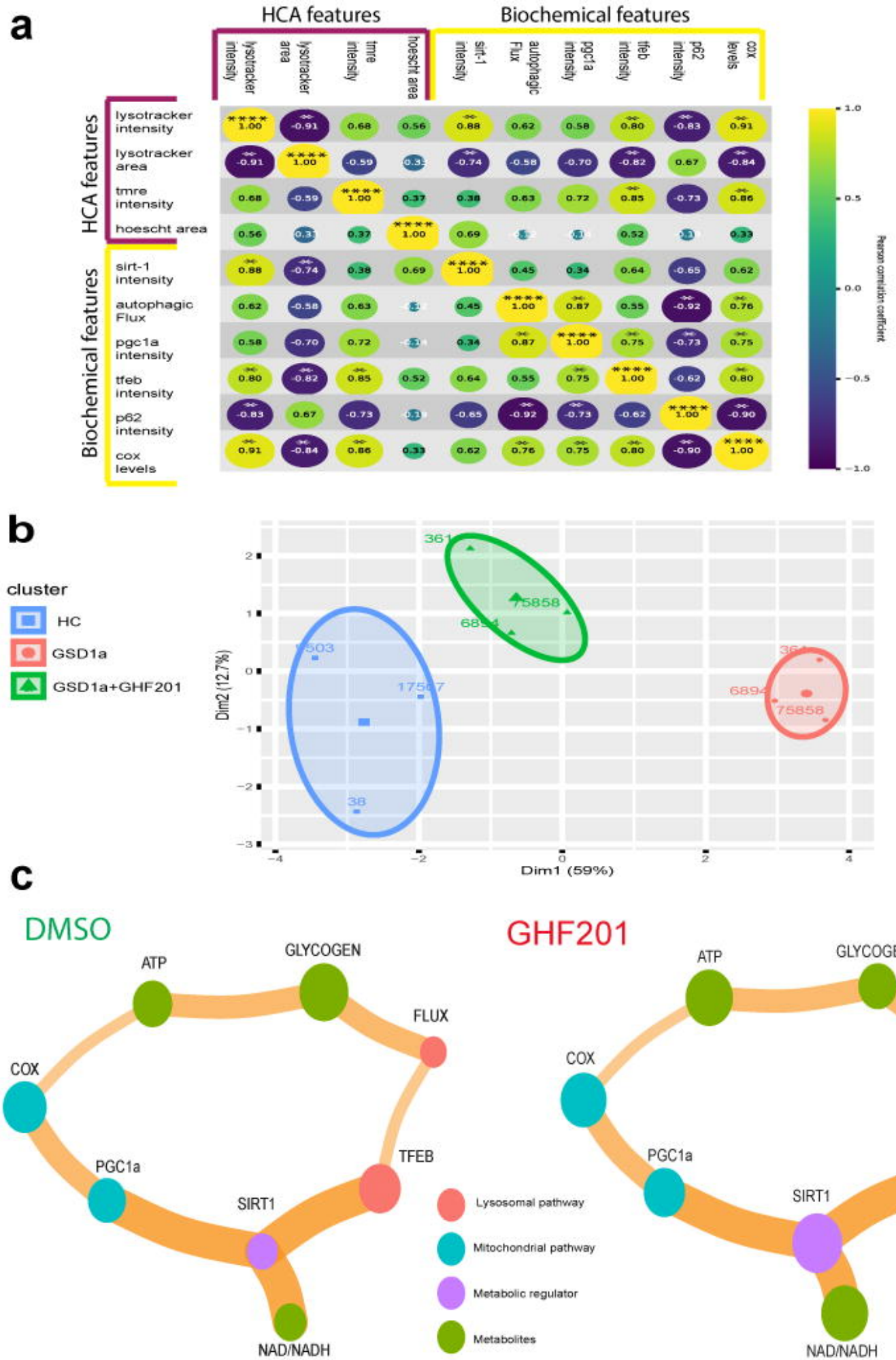
a
HCA features
Biochemical features
lysotracker intensity
lysotracker area
tmre intensity
hoescht area
sirt-1 intensity
autophagic Flux
pgc1a intensity
tfeb intensity
p62 intensity
cox levels
Pearson correlation coefficient
b
cluster
HC
GSD1a
GSD1a+GHF201
Dim1 (59%)
Dim2 (12.7%)
c
DMSO
GHF201
ATP
GLYCOGEN
FLUX
COX
PGC1a
TFEB
SIRT1
NAD/NADH
Lysosomal pathway
Mitochondrial pathway
Metabolic regulator
Metabolites

a

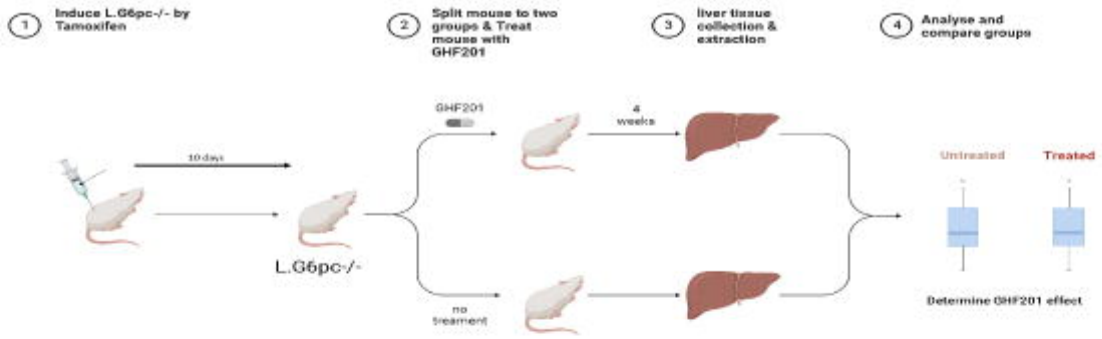
1 Induce L.G6pc-/- by Tamoxifen
2 Split mouse to two groups & Treat mouse with GHF201
3 liver tissue collection & extraction
4 Analyse and compare groups
10 days
L.G6pc-/-
GHF201
4 weeks
no treament
Untreated
Treated
Determine GHF201 effect

b

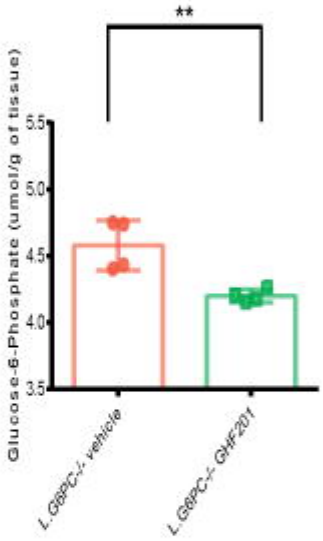
**
Glucose-6-Phosphate (umol/g of tissue)
5.5
5.0
4.5
4.0
3.5
L.G6PC-/- vehicle
L.G6PC-/- GHF201

c

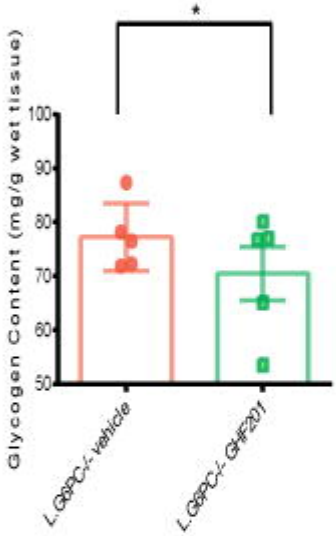
*
Glycogen Content (mg/g wet tissue)
100
90
80
70
60
50
L.G6PC-/- vehicle
L.G6PC-/- GHF201

d

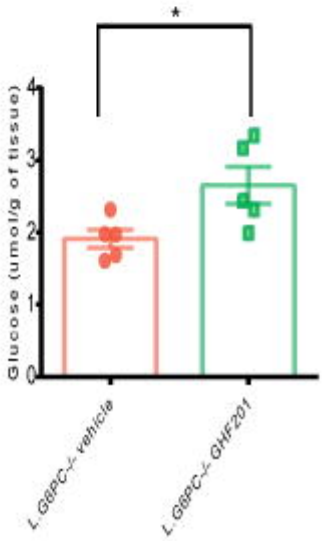
*
Glucose (umol/g of tissue)
4
3
2
1
0
L.G6PC-/- vehicle
L.G6PC-/- GHF201

e

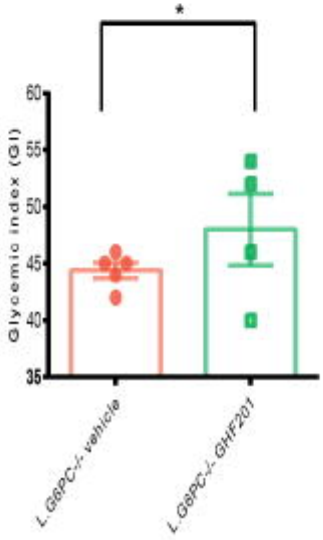
*
Glycemic index (GI)
60
55
50
45
40
35
L.G6PC-/- vehicle
L.G6PC-/- GHF201

f

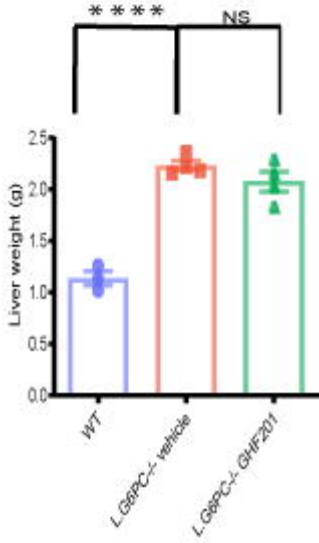
****
NS
Liver weight (g)
2.5
2.0
1.5
1.0
0.5
0.0
WT
L.G6PC-/- vehicle
L.G6PC-/- GHF201